Germanium–Tin/Cadmium Sulfide Core/Shell Nanocrystals with Enhanced Near-Infrared Photoluminescence

Brett W. Boote[†], Long Men[†], Himashi P. Andaraarachchi, Ujjal Bhattacharjee, Jacob W. Petrich, Javier Vela*, Emily A. Smith*

Affiliations

The Ames Laboratory, U.S. Department of Energy, and Department of Chemistry, Iowa State University, Ames, Iowa 50011-3111, United States

[†]*These authors contributed equally to this manuscript*

Abstract

$Ge_{1-x}Sn_x$ alloy nanocrystals and $Ge_{1-x}Sn_x$/CdS core/shell nanocrystals were prepared *via* solution phase synthesis and their size, composition, and optical properties were characterized. The diameter of the nanocrystal samples ranged from 6 to 13 nm. The crystal structure of the $Ge_{1-x}Sn_x$ materials was consistent with cubic diamond phase while the CdS shell was consistent with the zinc blende polytype. Inclusion of Sn alone does not result in enhanced photoluminescence intensity, however, adding an epitaxial CdS shell onto the $Ge_{1-x}Sn_x$ nanocrystals does enhance the photoluminescence up to 15× over Ge/CdS nanocrystals with a pure Ge core. More effective passivation of surface defects—and a consequent decrease in surface oxidation—by the CdS shell as a result of improved epitaxy (smaller lattice mismatch) is the most likely explanation for the increased photoluminescence observed for the $Ge_{1-x}Sn_x$/CdS materials. With enhanced photoluminescence in the near-infrared, $Ge_{1-x}Sn_x$ core/shell

nanocrystals might be useful alternatives to other materials for energy capture and conversion applications and as imaging probes.

Introduction

Ge-based materials have garnered significant attention recently as alternatives to other well-studied luminescent semiconductors, such as cadmium and lead chalcogenides.[1, 2] Materials made of elemental Ge have band gaps in the 0.67 to 1.6 eV range for bulk and highly confined (~2-3 nm) nanocrystals, respectively.[3] The large blue shift in the band gap of the nanocrystals is due to size-dependent quantum confinement. Though prone to oxidation when uncoated, Ge nanocrystals have been shown to exhibit increased stability as well as enhanced photoluminescence when a suitable shell is added.[4, 5]

Ge initially would seem to have limited utility in energy applications due to its inherent indirect band gap, which lowers its absorption cross-section and quantum yields. Recent reports suggest incorporation of Sn into Ge nanocrystals and thin films should produce a more direct band gap as a result of lattice strain.[6-8] For thin films, modifying the substrate on which the films are grown also allows the strain to be tuned while keeping the Sn composition constant.[9] A careful study of the bowing parameter on $Ge_{1-x}Sn_x$ films showed the crossover Sn content to be x = 0.087, which was higher than previously predicted.[10] It has also been shown by Senaratne *et al.* that n-type doping of $Ge_{1-x}Sn_x$ films enhances the photoluminescence.[11] Recently, Stange *et al.* demonstrated a strain-dependent indirect-to-direct band gap transition in $Ge_{0.875}Sn_{0.125}$ thin films grown on Ge buffer layers.[12] Band gap characteristics of related Ge-rich $Ge_{1-x}Si_x$ films have also been studied as a step toward the design of ternary systems based on Si, Ge, and Sn.[2]

Over the last decade, various methods to prepare Ge nanocrystals have been developed. Reduction of germanium halides ($GeCl_4$, $GeBr_2$, GeI_2 or GeI_4) using strong reducing agents ($NaBH_4$, $LiAlH_4$, etc.) in the presence of suitable surfactants [oleylamine, octadecene (ODE), trioctylphosphine (TOP)] is widely used to make monodisperse Ge nanocrystals.[13-22] Heating a solution of $GeBr_2$ or GeI_2 with a surfactant has also been shown to generate Ge nanocrystals.[23-25] Co-reduction of GeI_2 and GeI_4 is another common strategy for generating Ge nanocrystals in the ~2-20 nm size regime, where the precursor ratio controls the particle size.[3, 26-30] The polymerization of $[Ge_9]^{4-}$ or other related Zintl ions, both with and without linking cations such as Ge^{4+} or Pt^{2+}, generates highly ordered, porous Ge nanocrystals.[31-35] Other preparations involve reduction of Ge-rich oxides,[36-41] heat-assisted reduction of the GeH_2 Wittig adduct $Ph_3PCMe_2 \cdot GeH_2 \cdot BH_3$,[42, 43] laser photolysis of $Ge(CH_3)_4$ or GeH_4 gas,[44-46] photolysis of Ge wafer,[47] electroless deposition on preformed Ag nanocrystals,[48] Au-catalyzed vapor-liquid-solid growth using GeH_4[49] or diphenylgermane,[50] ultrasonic aerosol pyrolysis of tetrapropylgermane,[51] solution or solid phase reduction of NaGe,[52] plasma decomposition of $GeCl_4$[53-55] or GeH_4,[56] sulfur-assisted thermal decomposition of triphenylgermanium chloride,[57] and heating a solution of an alkylgermane in various high-temperature organic solvents.[58]

The preparation of Ge-Sn alloy nanocrystals typically follows one of the aforementioned strategies with the addition of a suitable Sn precursor, such as tin(II) chloride ($SnCl_2$) or bis(trimethylsilyl)amide $[Sn(HDMS)_2]$.[6, 59] A recent report showed the bottom-up formation of $Ge_{1-x}Sn_x$ nanowires grown from Sn nanocrystals.[60] The concentration of Sn in these nanowires was found to be 12.4 atom% ($x = 0.124$). $Ge_{1-x}Sn_x$ nanowires have also been formed from mixed Ge(II) and Sn(II) imido cubane precursors.[61] Spherical, Sn-rich Ge-Sn nanocrystals within a Ge matrix were prepared by annealing a Ge-Sn alloy layer cast between two thick layers of Ge.[62]

Small aspect ratio Ge-Sn nanorod heterostructures have been prepared in one-pot through sequential additions of Sn and Ge precursors.[63] There are also several reports on Ge-Sn alloy thin films to study strained and relaxed phases.[7, 9, 64, 65]

Raman spectroscopy is very useful for the characterization of multiple component inorganic materials. It can be used to characterize amorphous *vs.* crystalline materials[58] and to determine strain within alloy systems.[6, 60, 61] Lin *et al.* independently found the contributions of alloy composition and strain to the shift in the Ge-Ge longitudinal optical (LO) phonon in $Ge_{1-x}Sn_x$ films by tuning substrate topology.[9] They found a linear dependence between the Raman shift and film strain ($\Delta\omega = -(563 \pm 34)\varepsilon$ cm^{-1}) as well as Sn composition ($\Delta\omega = -(82 \pm 4)x$ cm^{-1}) where ε is the strain (in fractional form) and x is the Sn composition. Esteves *et al.* measured the Ge LO phonon mode by Raman spectroscopy for spherical $Ge_{1-x}Sn_x$ nanocrystals with increasing Sn content up to x = 0.279.[6] Increasing Sn content was associated with a lower Raman shift from ~294 to 287 cm^{-1}, which they attributed to combined alloy composition and lattice strain. Using Raman spectroscopy and scanning tunneling electron microscopy with energy dispersive X-ray spectroscopy (STEM-EDX), Seifner *et al.* correlated a shift in the LO phonon mode with varying Sn content for $Ge_{1-x}Sn_x$ nanorods.[61] A maximum shift in the LO phonon mode of -15 cm^{-1} was observed for nanorod sections where the mole fraction of Sn was at least 0.20. Similar behavior in $Ge_{1-x}Sn_x$ nanorods was observed by Biswas and coworkers.[50]

X-ray photoelectron spectroscopy (XPS) is another technique well suited to characterize Ge materials since they are prone to oxidation. XPS data for $Ge_{1-x}Sn_x$ nanocrystals synthesized by Ramasamy *et al.* showed typical peaks corresponding to Ge^0, Ge^{2+}, Ge^{4+}, Sn^0, and a broad, overlapping peak for Sn^{2+} and Sn^{4+}.[59] Relatively high ratios of the metallic peak to the oxidized peaks correlate to very little surface oxidation of these nanocrystals. Esteves and coworkers

observed similar results, where three types of peaks were present: metallic Ge^0 and Sn^0 peaks from interior atoms, Ge^{2+} and $Sn^{2+/4+}$ peaks from atoms bound to passivating ligands, and a small Ge^{4+}peak from GeO_2 at the surface.[6] It has also been shown by XPS that treating Ge nanocrystals with dilute HCl removed a high percentage of a GeO_2 layer at the surface, with weakly bound Cl^- acting as a passivating ligand.[45] Indeed, all reports on the preparation of Ge nanocrystals where XPS was performed show strong peaks for Ge^0 and small contributions from oxidized species, whether they are attributed to surface ligands and/or surface oxidation (GeO_2).[19, 29, 66]

The photoluminescence (PL) properties of Ge-based materials are highly sensitive to the resultant size of the nanocrystals as well as other properties such as the capping ligand used.[3, 4, 18, 53, 67] Lee *et al.* prepared Ge nanocrystals stabilized with 1-octadecene that exhibited luminescence maxima from 900 to 1400 nm for diameters 3.2 to 4.0 nm.[18] Ruddy and coworkers demonstrated luminescent 2.3-4.7 nm nanocrystals capped with 1-octadecene prepared by co-reduction of GeI_2 and GeI_4 with size-dependent near-infrared PL from 860-1230 nm.[3] Guo *et al.* demonstrated 7 nm Ge/4.9CdS core/shell nanocrystals that exhibited a PL maximum at 950 nm.[4] Wheeler and coworkers showed 4.8-10.2 nm Ge nanocrystals capped with alkyl chains synthesized in the vapor phase that exhibit PL from 1200-1610 nm.[53] Recently, Robel and coworkers monitored the combined effect of temperature and high magnetic field on the PL lifetimes of Ge nanocrystals, which showed splitting between closely-spaced states as well as mixing between dark and bright states all contribute toward the indirect PL.[67] The intricacies of these widely varying optical properties are not clear: surface states very likely play a role for the luminescence in the visible region, as this extent of a blue shift from the bulk band gap is not explained by confinement alone.

Temperature-dependent PL studies have also been performed to examine the direct and indirect band gap contributions of $Ge_{1-x}Sn_x$ materials.[68, 69] The Arachchige group has demonstrated highly confined $Ge_{1-x}Sn_x$ nanocrystals showing PL in the 620 to 770 nm range, which closely follow calculations using *ab initio* HSE hybrid functional theory. They also used time-resolved PL at low (15 K) and ambient temperatures to further understand carrier dynamics.[70, 71] PL lifetimes at 15 K were found to be 3-27 μs, three orders of magnitude slower than at room temperature, owing to slow recombination of carriers in surface traps and spin-forbidden dark excitons. Temperature effects on the PL of very thin $Ge_{1-x}Sn_x$ films have also been studied, showing a monotonic thermal PL quenching despite the indirect nature of the band gap.[72]

Reported herein are the comparative solution phase synthesis, characterization, and optical properties of $Ge_{1-x}Sn_x$ alloy nanocrystals *vs.* $Ge_{1-x}Sn_x$/CdS core/shell nanocrystals. All nanocrystalline samples were characterized by X-ray diffraction (XRD), transmission electron microscopy (TEM), Raman spectroscopy, X-ray photoelectron spectroscopy (XPS), and steady-state and time-resolved near infrared PL spectroscopy. The purpose of this work is to better understand the photophysical properties of Sn-doped Ge-based nanocrystals that may be useful for energy-related applications such as photovoltaics, light emitting devices (LEDs) or, with appropriate surface passivation,[73, 74] as near-infrared active luminescent biological markers.

Experimental

Materials. Cadmium oxide (CdO, 99.998%), sulfur (S_8, 99.999%) and oleic acid (90%) were purchased from Alfa Aesar; *n*-butyllithum (*n*-BuLi, 1.6 M hexane solution), bis[bis(trimethylsilyl)amido]tin(II) ($Sn(HMDS)_2$, ≥99.0%), oleylamine (OLA, ≥80-90.0%) and dioctylamine ($octyl_2NH$, 98%) were purchased from Sigma-Aldrich; hexadecylamine

(hexadecylNH_2, 98%) and 1-octadecene (ODE, 90%) were purchased from Acros; and germanium(II) iodide (GeI_2, 99.99+%-Ge) was purchased from Strem. Procedures were performed under a dry inert gas atmosphere (N_2 or Ar) inside a glovebox or Schlenk line, unless specified otherwise.

Preparation of Ge and $Ge_{1-x}Sn_x$ (core) nanocrystals. Germanium cores were synthesized by a modified literature procedure.[4] Briefly, GeI_2 (0.049 g, 0.15 mmol) was added to an oven-dry, four-neck 250 mL round-bottom (R.B.) flask containing hexadecylamine (0.75 g, 3.1 mmol). The contents were degassed under vacuum at 80°C for 30 min, refilled with dry Ar, and heated to 200°C. A mixture of n-BuLi (0.2 mL of 1.6 M hexane solution) and ODE (0.75 mL) was quickly injected while stirring. The temperature was raised from 200°C to 300°C, and the mixture further stirred for 1 h before cooling to room temperature (R.T., 21°C). The nanocrystals were purified by crashing three times with 10 mL of a 1:1 or 1:3 v/v acetone/methanol solution and centrifugation at 4500 rpm for 5 min, followed by redispersion in 5 mL of toluene.

$Ge_{1-x}Sn_x$ cores were prepared by a modified reported procedure.[59] Briefly, GeI_2 (0.049g, 0.15 mmol) and oleylamine (5 mL for $Ge_{0.95}Sn_{0.05}$; 10 mL for $Ge_{0.75}Sn_{0.25}$) with a varied amount of $Sn(HMDS)_2$ (0.018 g, 0.04 mmol for $Ge_{0.95}Sn_{0.05}$; 0.066 g, 0.15 mmol for $Ge_{0.75}Sn_{0.25}$) were added into a four-neck 250 mL round-bottom flask in a glovebox. The mixture was degassed under vacuum at 80 °C for 30 min, refilled with dry Ar, and heated to 230 °C for $Ge_{0.95}Sn_{0.05}$ or 280°C for $Ge_{0.75}Sn_{0.25}$. The mixture was annealed for 30 min for $Ge_{0.95}Sn_{0.05}$ cores or 5 min for $Ge_{0.75}Sn_{0.25}$ cores before cooling down to R.T.. It should be noted that the exact compositions of $Ge_{1-x}Sn_x$ nanocrystals varied somewhat from batch to batch; the low Sn inclusion preparation varied from 4-8% Sn, while the high Sn inclusion preparation varied from 23-28%. For simplicity, these are labeled as $Ge_{0.95}Sn_{0.05}$ and $Ge_{0.75}Sn_{0.25}$, respectively.

Preparation of Ge/CdS and $Ge_{1-x}Sn_x$/CdS (core/shell) nanocrystals. Ge/CdS or $Ge_{1-x}Sn_x$/CdS core/shell nanocrystals were prepared as follows: precursor solutions of Cd and S were prepared by a literature procedure.[4] 0.1 M $Cd(oleate)_2$ solution: CdO (318 mg, 2.48 mmol), oleic acid (3.09 g, 10.9 mmol), and ODE (7.11 g, 28.2 mmol) were degassed under vacuum at 80°C for 60 min, refilled with Ar, and heated to 240°C until optically clear. The mixture was allowed to cool down to R.T., and $(octyl)_2NH$ (12.5 mL, 41.4 mmol), previously degassed at 80°C for 30 min, injected into it. 0.1 M S_8 solution: S_8 (79.0 mg, 2.47 mmol) and ODE (19.7 g, 78.1 mmol) were degassed under a vacuum at 80°C for 30 min, refilled with Ar, and heated to 180°C for 20 min until optically clear.

To prepare core-shell nanocrystals *with excess precursors* (one-pot synthesis), a batch of freshly prepared $Ge_{1-x}Sn_x$ cores (in amine or amine/ODE) solution, ODE (1.5 mL, 4.7 mmol), and $(octyl)_2NH$ (1.5 mL, 5.0 mmol) were added to a four-neck 250 mL R.B. flask. The mixture was degassed at 80°C for 30 min, refilled with Ar, and heated to 230°C for Ge and $Ge_{0.95}Sn_{0.05}$ or 250°C for $Ge_{0.75}Sn_{0.25}$). Cd and S precursors were alternately injected using two programmable syringe pumps, each followed by a 15 min wait. The S precursor was injected first. 15 min after the last Cd injection, the mixture was allowed to cool to R.T.. Core-shell nanocrystals were washed as described above for $Ge_{1-x}Sn_x$ nanocrystals.

To prepare core-shell nanocrystals *without excess precursors*, the procedure above was repeated using nanocrystal cores where excess precursors have been removed following the purification method above. Toluene was removed under vacuum prior to shell growth.

Optical Characterization. Solution optical density (absorption plus scattering) spectra were measured with a photodiode array 8453 UV-visible spectrophotometer (Agilent, Santa Clara, CA). Steady-state photoluminescence (PL) spectra were measured using a Horiba-Jobin

Yvon Nanolog scanning spectrofluorometer equipped with a liquid nitrogen-cooled InGaAs photodiode array. To account for sample concentration, PL intensities were divided by the optical density at the excitation wavelength of 350 nm. Photoluminescence lifetime measurements were performed using a previously described setup with a Nd:YAG laser (Continuum) and an avalanche photodiode.[75] The samples in toluene solution were excited at 532-nm with a pulse energy of 1 mJ/cm^2. The time-resolved photoluminescence was collected using an 800-nm long-pass filter and the decay trace was fit to a single or double exponential decay as needed.

Raman microspectroscopy was performed on nanocrystals using a 532-nm Sapphire SF laser (Coherent, Santa Clara, CA) illuminating a DM IRBE inverted light microscope (Leica Microsystems, Buffalo Grove, IL) fitted with a 100× oil (1.47 NA) objective. The nanocrystal solutions were drop cast onto glass slides and dried under ambient conditions. The scattered light was passed into a HoloSpec spectrometer (Kaiser Optical Systems, Ann Arbor, MI) equipped with a Newton 940 CCD camera (Andor Technology, Belfast, United Kingdom). The laser power density was 1.3×10^4 W/cm^2 with a laser spot size of 1 μm, and the acquisition time was 60 s. The data were plotted using IGOR (WaveMetrics, Portland, OR).

Infrared spectroscopy was performed on a Bruker Vertex 80 FT-IR spectrometer equipped with a MIR_IR_XPM detector with 16 scans at a resolution of 4 cm^{-1}. The samples were prepared as drop cast thin films on NaCl salt plates. Background spectra were collected under identical conditions, and samples were continuously purged with dry N_2 to minimize water vapor absorbance.

Structural Characterization. Powder X-ray diffraction (XRD) was measured using Cu Kα radiation on a Rigaku Ultima diffractometer. X-ray photoelectron spectroscopy (XPS)

measurements were performed using a Kratos Amicus/ESCA 3400 instrument. The sample was irradiated with 240 W non-monochromated Mg Kα x-rays, and photoelectrons emitted at 0 ° from the surface were analyzed using a DuPont-type analyzer. The pass energy was set at 75 eV. CasaXPS was used to process raw data files. The binding energy of C 1s at 284.6 eV was used as a reference. Depth profiling was performed using monoatomic Ar ion sputtering for 8 s, followed by XPS acquisition. The acceleration voltage used was 500 V in order to minimize ion-induced reduction. Sample rotation during sputtering was used to achieve uniform etching. Transmission Electron Microscopy (TEM) was conducted using a FEI Tecnai G2 F20 field emission TEM operating at up to 200 kV. Samples were prepared by placing 1 or 2 drops of concentrated toluene solutions onto carbon-coated copper grids. Elemental composition was characterized by energy-dispersive spectroscopy (EDX). Nanocrystal dimensions were measured with ImageJ. The longest dimension was measured and reported. At least 300 nanocrystals were counted in each case. Uncertainties in all measurements are reported as standard deviations.

Results and Discussion

Synthesis and Characterization of $Ge_{1-x}Sn_x$ Core Nanocrystals. Ge, $Ge_{0.95}Sn_{0.05}$, and $Ge_{0.75}Sn_{0.25}$ nanocrystals were prepared and characterized by powder X-ray diffraction (XRD). Patterns of $Ge_{1-x}Sn_x$ nanocrystals shown in **Figure 1** confirm the crystalline products are homogeneous nanoalloys of Ge and α-Sn in the cubic diamond phase with $Fd\overline{3}m$ space group. The composition of Sn incorporated in the cubic Ge lattice was calculated based on Vegard's Law: $a_{(Ge_{1-x}Sn_x)} = a_{(Sn)}(x) + a_{(Ge)}(1-x)$. Here, a is the lattice parameter of the sample or standard and x is the composition of Sn in the nanocrystal. Structural parameters of the Ge and $Ge_{1-x}Sn_x$ nanocrystals, as well as CdS, are shown in **Table 1** and **Figure 2**. The shift in the diffraction peak to lower 2θ angles indicates a lattice expansion from 5.658 Å (Ge) to 5.706 Å

($Ge_{0.95}Sn_{0.05}$) and 5.870 Å ($Ge_{0.75}Sn_{0.25}$). To ensure the measured peak shift was not due to any measurement variables, such as the sample height in the XRD instrument, Si powder was used as an internal standard to align the experimental pattern for all samples. As is often the case in low temperature, solution-synthesized nanocrystals,[5] the molar ratios of Ge:Sn used in the synthetic preparations were not conserved in the nanocrystal. For instance, the $Ge_{0.75}Sn_{0.25}$ sample was prepared from a 1:1 molar ratio of Ge:Sn. This could be explained, in part, by the comparatively large cationic radius of Sn^{2+} compared to Ge^{2+}, which contributes to Sn having a relatively low solubility in bulk Ge of about ~1%.[76] However, Sn incorporation as high as 42% has been reported in $Ge_{1-x}Sn_x$ nanocrystal alloys,[59] likely because solution phase nanocrystal syntheses are often kinetically and not thermodynamically controlled.

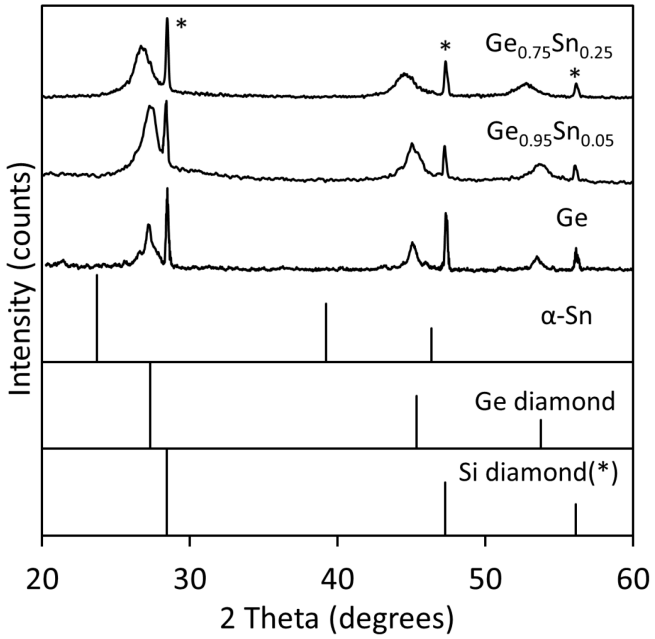

Figure 1. Experimental powder X-ray diffraction (XRD) patterns of Ge and $Ge_{1-x}Sn_x$ alloy nanocrystals. The standard powder XRD patterns of bulk Ge, α-Sn, and Si diamond (* = used as an internal standard) are shown for comparison.

Table 1. Structural parameters of Ge and $Ge_{1-x}Sn_x$ nanocrystals.

Material	Crystal structure	Lattice parameter (Å)	Lattice mismatch[a]
CdS	zinc blende	5.832	0
Ge	diamond	5.658	+3.0%
$Ge_{0.95}Sn_{0.05}$	diamond	5.706	+2.2%
$Ge_{0.75}Sn_{0.25}$	diamond	5.870	-0.65%

[a] $\Delta a = 100 \times (a_{shell} - a_{core})/(a_{core})$; signs refer to shell-induced core expansion (+) or compression (-).

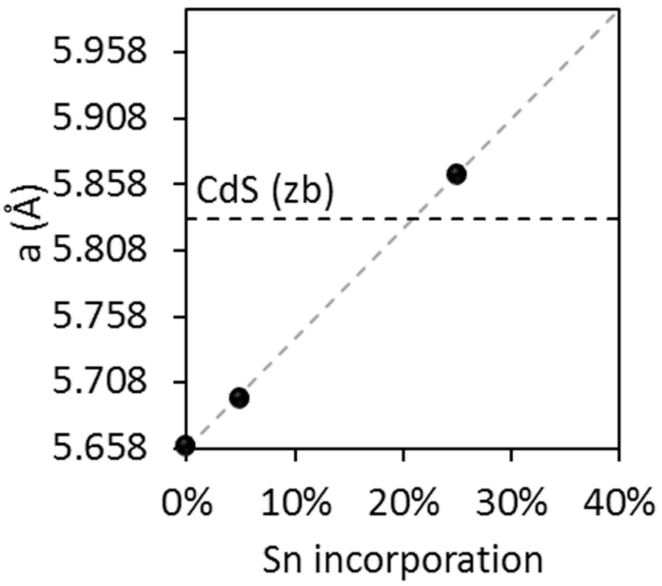

Figure 2. Lattice parameter of $Ge_{1-x}Sn_x$ nanocrystals as a function of Sn incorporation. $Ge_{0.75}Sn_{0.25}$ nanocrystals have the smallest lattice mismatch with the cubic CdS (5.832, horizontal dashed line), compared to Ge or $Ge_{0.95}Sn_{0.05}$. The dashed gray line is a linear regression to the data.

To accurately characterize the morphology and size of the nanocrystals, TEM images were collected (**Figure 3**). Size histograms for each sample are shown in **Figure S1**. Overall, the samples are well dispersed spheroidal nanocrystals with crystal sizes of 6 ± 1 nm (Ge), 6 ± 1 nm ($Ge_{0.95}Sn_{0.05}$), and 11 ± 2 nm ($Ge_{0.75}Sn_{0.25}$). Adding more Sn precursor always leads to larger core particles. In an effort to make $Ge_{1-x}Sn_x$ cores comparable in size to Ge cores, we lowered the precursor solution concentration and shortened the reaction time. However, while this approach works well for $Ge_{0.95}Sn_{0.05}$ with a particle size of 6 ± 1 nm, the smallest $Ge_{0.75}Sn_{0.25}$ we could synthesize still has a relatively large particle size of 11 ± 2 nm. In addition to TEM, energy dispersive spectrometry (EDX) was performed to assess the particle composition and

homogeneity (**Table 2**). EDX data of $Ge_{1-x}Sn_x$ nanocrystals shows good agreement with the theoretical elemental composition calculated by Vegard's Law.

Table 2. TEM-EDX analysis of Ge, $Ge_{1-x}Sn_x$ and $Ge_{1-x}Sn_x$/CdS nanocrystals.

Sample	Size (nm)	Composition: Ge, Sn, Cd, S	
		Theoretical (%)[a]	EDX (%)
Ge	6 ± 1	100, 0, 0, 0	100, 0, 0, 0
$Ge_{0.95}Sn_{0.05}$	6 ± 1	95, 5, 0, 0	90 ± 1, 10 ± 1, 0, 0
$Ge_{0.75}Sn_{0.25}$	11 ± 2	75, 25, 0, 0	78 ± 3, 22 ± 3, 0, 0
Ge/3.4CdS	8 ± 2	19, 0, 41, 41	7 ± 1, 0, 49 ± 1, 44 ± 1
$Ge_{0.95}Sn_{0.05}$/3.4CdS	8 ± 2	29, 2, 35, 35	67 ± 9, 8 ± 7, 18 ± 8, 7 ± 3
$Ge_{0.75}Sn_{0.25}$/3.4CdS	13 ± 2	28, 9, 31, 31	58 ± 3, 4 ± 2, 16 ± 2, 22 ± 1

[a]Based on a 100% Ge_xSn_{1-x}/CdS composition.

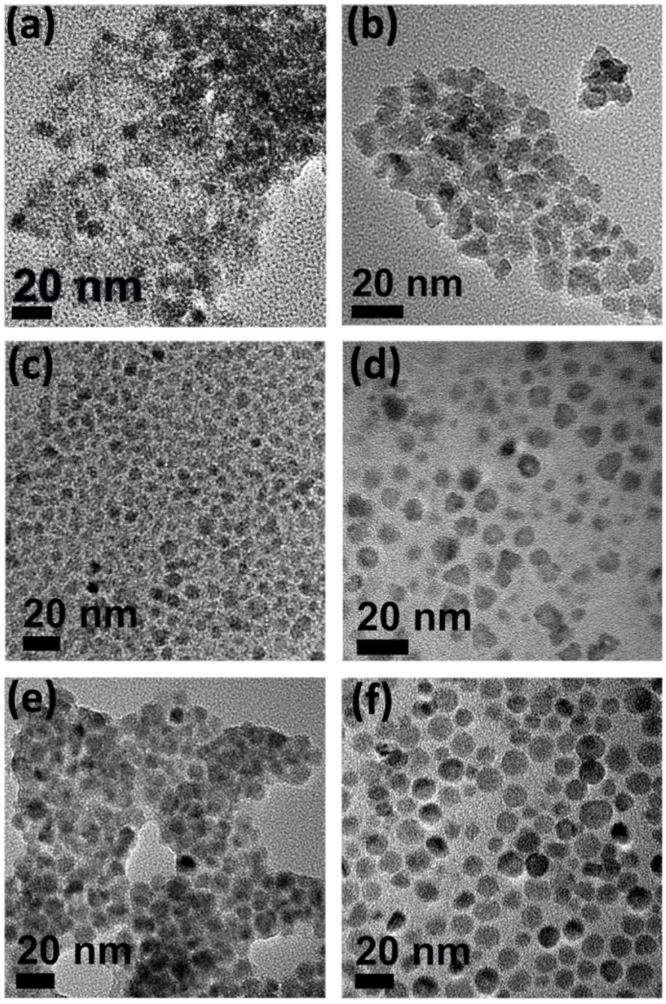

Figure 3. $Ge_{1-x}Sn_x$ core and $Ge_{1-x}Sn_x$ /CdS core/shell nanocrystals: (a) Ge (6 ± 1 nm), (b) Ge/CdS (8 ± 2 nm), (c) $Ge_{0.95}Sn_{0.05}$ (6 ± 1 nm), (d) $Ge_{0.95}Sn_{0.05}$/CdS (8 ± 2 nm), (e) $Ge_{0.75}Sn_{0.25}$ (11 ± 2 nm), (f) $Ge_{0.75}Sn_{0.25}$/CdS (13 ± 2 nm). The average size measured from more than 300 nanocrystals is provided in parentheses.

Raman spectra for the Ge-Ge LO phonon mode of pure Ge and $Ge_{1-x}Sn_x$ alloy nanocrystals are shown in **Figure 4a**. As the Sn content is increased, the Ge LO phonon mode is shifted by -1.2 cm^{-1} ($Ge_{0.95}Sn_{0.05}$) and -4.4 cm^{-1} ($Ge_{0.75}Sn_{0.25}$). For the $Ge_{1-x}Sn_x$ alloy system, two additive factors determine the observed peak shift in the Ge-Ge LO phonon: the compositional (pure mass) effect and lattice strain. Deconvoluting the compositional effect and strain has been performed on films, where substrate conditions allow for tuning the strain.[9, 64, 65, 77, 78] For small nanocrystals it is likely that the compositional effect dominates since strain within the alloy can be dissipated due to a high surface area.[50] The smaller Raman shifts are thus primarily attributed to the larger Sn atoms expanding the crystal lattice as shown by XRD; longer (weaker) bonds are associated with a shift to lower energies. A plot of the Sn compositional dependence of the Ge-Ge LO phonon is shown in **Figure 4b**. For two batches of $Ge_{1-x}Sn_x$ nanocrystals prepared in the same way the best-fit line produced different slopes despite similar compositions being measured by XRD: $\Delta\omega(x) = -(17 \pm 1)x$ and $\Delta\omega(x) = -(42 \pm 5)x$ where x is the Sn composition. At present, it is unclear why the two sets of experiments showed different compositional dependence, and why these values are different than those reported for nanorods[50] and strain-free films[65]—further experiments are underway to investigate this. The line traces shown in **Figure 4a** are two-peak Gaussian fits to the experimental spectra to account for asymmetry at lower Raman shifts. Asymmetry in the phonon peaks of small nanocrystals is attributed to contributions from surface optical (SO) phonons, which are typically slightly lower in energy than the corresponding LO phonons.[79, 80] SO phonons are more prominent for anisotropic crystals.[81] The Sn-Ge LO phonon was not observed in the Raman spectrum of the nanoalloy, which is consistent with previous

work on thin films.[65] A Raman spectrum of GeO_2 was also acquired to investigate the possibility of interference from surface oxidation (**Figure S2**), but no GeO_2 bands are observed in the 280 to 320 cm^{-1} Ge-Ge LO phonon range, which is consistent with the literature.[82] Likewise, no additional bands that correlate to GeO_2 were observed outside this spectral range for the Ge and $Ge_{1-x}Sn_x$ nanocrystal samples.

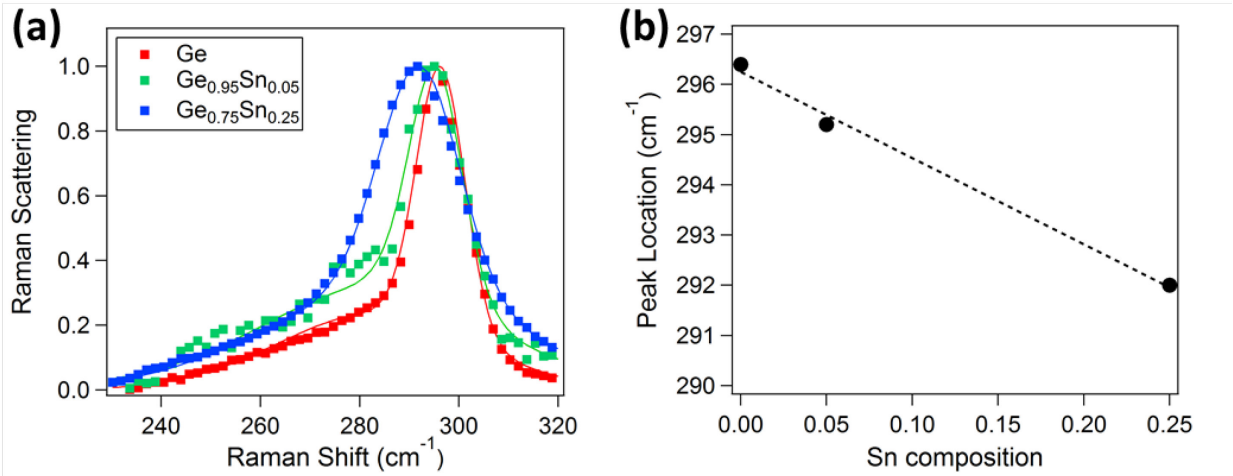

Figure 4. (a) Normalized Raman spectra for Ge and $Ge_{1-x}Sn_x$ alloy nanocrystals and (b) Sn compositional dependence of Ge-Ge LO phonon peak position. As the Sn content increases, the Ge LO phonon peak is shifted to lower wavenumbers and the FWHM increases. Spectra were fit to 2-peak Gaussian curves (solid lines) to account for asymmetry. Average Raman peak properties are listed in Table S1.

Synthesis and Characterization of $Ge_{1-x}Sn_x$/CdS Core/Shell Nanocrystals. Freshly synthesized $Ge_{1-x}Sn_x$ cores were reacted with Cd and S precursors alternately to form CdS shells using the successive ion layer adsorption and reaction (SILAR) method.[4, 83] Two preparation methods were employed: one using the synthetic mixture of the $Ge_{1-x}Sn_x$ cores without removing the residual precursors (one-pot synthesis), referred to as the crude $Ge_{1-x}Sn_x$ sample, and the second using cores re-suspended in toluene after purification *via* centrifugation, referred to as the purified $Ge_{1-x}Sn_x$ sample. The XRD patterns and Raman spectra of the crude $Ge_{1-x}Sn_x$ samples

showed unwanted SnS (**Figure S3**). Because the core/shell synthesis using crude core solutions did not generate monodisperse core/shell nanocrystals, all core/shell samples discussed in the remaining text were prepared using purified cores. **Figure 5** shows XRD patterns of the core/shell nanocrystals. The Ge/CdS sample showed mainly hexagonal wurtzite structure. Ge/CdS nanocrystals with a predominately wurtzite structure have been reported previously for a preparation using crude core solution.[4] Polytypism in group IV and II-VI nanocrystals, as well as in their epitaxial (core/shell, etc.) systems is relatively common, and can be size-dependent.[84-86]

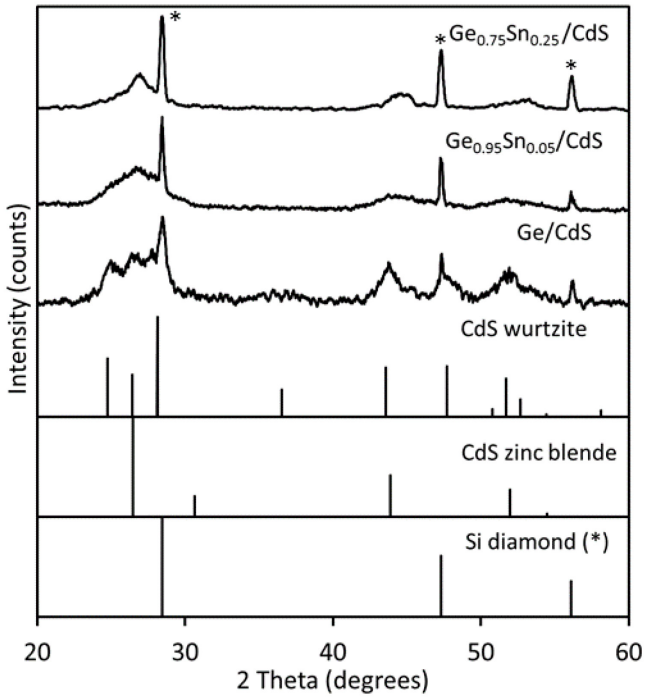

Figure 5. Experimental powder X-ray diffraction (XRD) patterns of Ge/CdS and $Ge_{1-x}Sn_x$/CdS core/shell nanocrystals. The standard powder XRD patterns of bulk CdS zinc blende (cubic), CdS wurtzite (hexagonal), and Si diamond (* = used as an internal standard) are shown for comparison.

To make the core/shell nanocrystals with different Sn incorporations comparable, we grew CdS shells with similar thicknesses. TEM images in **Figure 3** show, in all cases, the core/shell nanocrystals increase 2 nm in diameter compared to their uncoated or bare cores.

When compared to the known lattice parameter of CdS (either wurtzite or zinc blende give similar results), this shell thickness corresponds to the growth of 3.4 monolayers of CdS on the $Ge_{1-x}Sn_x$ cores. Area EDX scans containing several $Ge_{1-x}Sn_x$ cores agree with their theoretical elemental composition; albeit the Ge content in $Ge_{1-x}Sn_x$ /CdS core/shells appears to be larger than the theoretical value. EDX elemental mapping of individual particles show that a majority of $Ge_{1-x}Sn_x$ cores are coated with CdS (**Figure S4**). Many of these core/shell particles have a relatively inhomogeneous shell, which is consistent with well-documented studies on CdSe/CdS core/shell nanocrystals.[73, 74, 87-89]

As in the classical CdSe/CdS system, inhomogeneous surface coverage in $Ge_{1-x}Sn_x$ /CdS core/shell nanocrystals is not an immediate problem, at least in terms of ensemble optical properties, as it is able to provide enough surface passivation to enhance and stabilize PL compared to the bare $Ge_{1-x}Sn_x$ cores. High resolution high-angle annular dark-field (HAADF) STEM images of a $Ge_{0.75}Sn_{0.25}$/CdS nanocrystals (**Figure S5**) show the presence of continuous lattice fringes throughout each particle.

Raman spectra for the $Ge_{1-x}Sn_x$/CdS core/shell nanocrystals are shown in **Figure S6**. The Raman shift of the Ge-Ge LO phonon mode for the Ge/CdS nanocrystals is shifted by a statistically significant +1.1 cm^{-1} relative to the nanocrystals without a shell. This implies the shell generates compressive strain on the core, due to the smaller lattice parameter of CdS wurtzite compared to Ge (Ge = 5.658 Å, CdS wurtzite a = 4.135 Å). If CdS (with a peak maximum at 300 cm^{-1}) spectrally interfered with the Ge LO optical phonon mode (with a peak maximum <296 cm^{-1} in the core material), we would expect the peak FWHM to increase. We conclude that CdS does not spectrally interfere in our data, as the peak FWHM is the same or slightly decreased for the core/shell nanocrystals. In addition, no peaks were measured for pure

CdS nanocrystals measured under similar acquisition parameters as those used to collect the data in **Figure S6**. For the $Ge_{1-x}Sn_x$ core/shell samples, the shifts in the LO phonon mode upon shell addition are insignificant (**Table S1**). The lattice parameter for CdS zinc blende (5.82 Å) is closer to the lattice parameter of the alloy core materials (**Table 1**), particularly $Ge_{0.75}Sn_{0.25}$, which is consistent with minimal compressive strain and a negligible phonon mode shift. The smaller lattice mismatch between the $Ge_{1-x}Sn_x$ core nanocrystals and the CdS shell facilitates epitaxial growth of the latter.

X-Ray Photoelectron Spectroscopy of Ge/CdS and $Ge_{1-x}Sn_x$/CdS Core/Shell Nanocrystals. XPS survey spectra of all core/shell nanocrystal samples are shown in the supporting information (**Figure S7**). XPS depth profiling was performed to reveal the sub-surface information of the Ge/CdS core/shell nanocrystals and to corroborate the formation of a core/shell structure (**Figure 6**). We analyzed the chemical states of Ge, Cd, and S. There is no Ge signal above the noise in the initial etching cycles. After a few etching cycles, emerging peaks at ~29.5 eV in the Ge 3d energy region and ~1217 and 1250 eV in the Ge 2p energy region that correspond to metallic Ge^0 were measured, along with a shoulder peak at ~32-33 eV corresponding to $Ge^{2+/4+}$ (**Figure 6a**). These data are consistent with the chemical state of purified Ge core without any shell growth (Ge^0), which exhibits a peak at ~29.5 eV, and mild surface oxidation ($Ge^{2+/4+}$). Furthermore, the core/shell nanocrystals exhibited peaks throughout the etching at ~405 and ~412 eV corresponding to Cd, and a peak at ~162 eV, which corresponds to S^{2-} (**Figure 6c-d**). This substructure information provides confirmation for the chemical speciation of the core/shell structure of Ge/CdS nanocrystals.

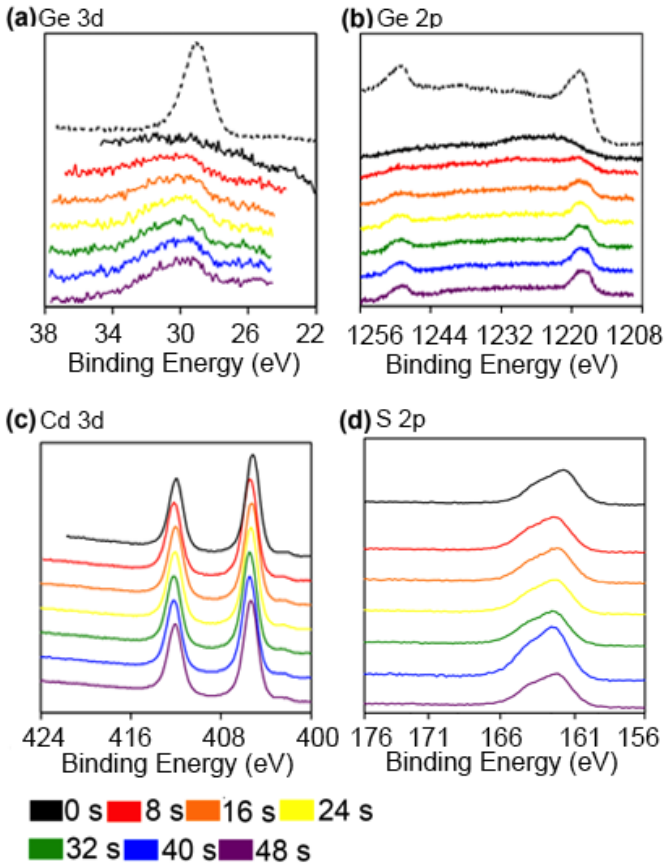

Figure 6. XPS depth profiles of Ge/CdS core/shell nanocrystals. Depth profiling uses an ion beam to etch the layers of the sample revealing sub-surface information; each etching cycle is 8 s and total etching time is indicated by the color of the spectra. Ge nanocrystals with no shell are shown as dashed lines in (a) and (b) for reference, and all the spectra are calibrated to adventitious carbon at 284.6 eV.

We similarly analyzed the chemical states of Ge, Sn, Cd, and S in the purified $Ge_{1-x}Sn_x$ and $Ge_{1-x}Sn_x$/CdS core/shell nanocrystals (**Figure 7**). XPS confirms the element distribution in alloy nanocrystals. The Ge 3d peak at ~29.5 eV and a shoulder around ~32-33 eV corresponds to Ge^0 and $Ge^{2+/4+}$ species, respectively. The peak at ~486 eV corresponds to Sn^{4+} species (SnO_2). Ge and Sn in higher oxidation states indicate post-synthetic surface oxidation. The core/shell

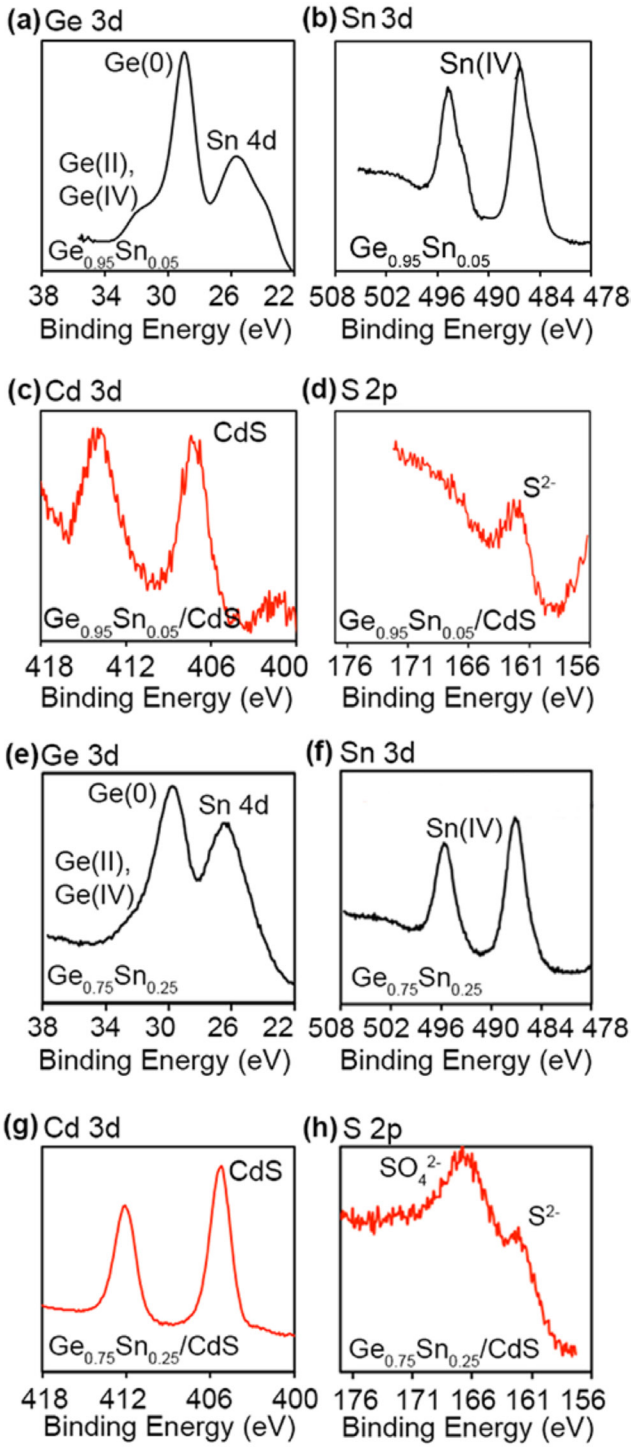

Figure 7. X-ray photoelectron spectra (XPS) of (a-b) $Ge_{0.95}Sn_{0.05}$, (c-d) $Ge_{0.95}Sn_{0.05}$/CdS, (e-f) $Ge_{0.75}Sn_{0.25}$, and (g-h) $Ge_{0.75}Sn_{0.25}$/CdS nanocrystals. All the spectra are calibrated to adventitious carbon at 284.6 eV.

Luminescence Properties of $Ge_{1-x}Sn_x$ Core and $Ge_{1-x}Sn_x$/CdS Core/Shell Nanocrystals.

The solution phase optical density spectra of Ge and $Ge_{1-x}Sn_x$ nanoscrystals show no prominent absorption features (**Figure 8**), which could be due to the small bandgap (0.66 eV, 1876 nm for bulk Ge, **Figure S8**) being out of our instrument range. The $Ge_{1-x}Sn_x$/CdS core/shell nanocrystals have absorption onsets at 450-500 nm, which is consistent with the bandgap of quantum confined CdS shells (**Figure S8**).[90]

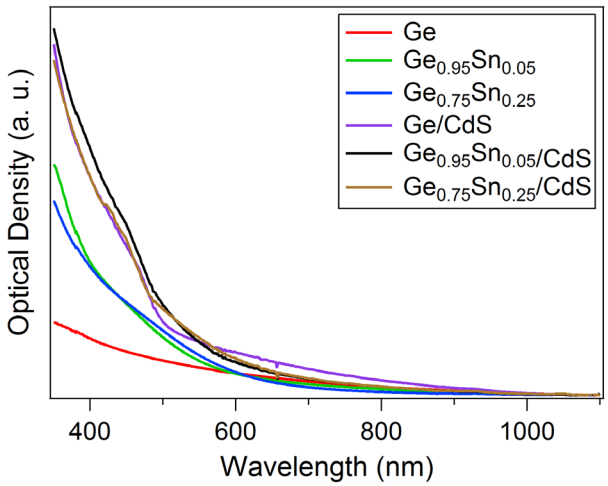

Figure 8. Solution phase optical density (absorption and scattering) spectra of Ge, $Ge_{1-x}Sn_x$, Ge/CdS and $Ge_{1-x}Sn_x$/CdS nanocrystals suspended in toluene.

Photoluminescence spectra of the nanocrystals corrected for optical density at the excitation wavelength of 350 nm are shown in **Figure 9**. For the nanocrystals without shells, the signals from all samples were too low to confidently discriminate them from the instrument's background. This means there is no detectable PL from any of the core-only nanocrystals. Sn inclusion in the alloy nanocrystals is thus not associated with an increase in luminescence intensity. Assuming the doped and undoped samples had similar surface defects and surface oxidation, there is no indication that a more direct band gap character was achieved in the Sn-doped nanocrystals, as an enhanced PL response was not measured. On the other hand, all the core/shell nanocrystals

display an enhanced near infrared PL compared to the $Ge_{1-x}Sn_x$ and Ge nanocrystals without shells. With a bulk band gap of 0.66 eV (**Figure S8**), the PL spectra indicate these core/shells are also quantum confined. The PL enhancements of $Ge_{0.75}Sn_{0.25}$/CdS and $Ge_{0.95}Sn_{0.05}$/CdS were 15× and 12× greater than Ge/CdS, respectively. The luminescence intensity decreases when oxidation is measured by the presence of a Ge-O band in the FT-IR spectrum. $Ge_{0.75}Sn_{0.25}$/CdS core/shells where no oxidation was present show the highest PL intensity. In another set of experiments where oxidation was measured by FT-IR spectroscopy (for example **Figure S9** shows an example of oxidation in the $Ge_{0.75}Sn_{0.25}$ sample), the oxidized core/shells exhibited 100× lower luminescence than the non-oxidized $Ge_{0.75}Sn_{0.25}$/CdS sample (**Figure 9**). The observed PL enhancement is most likely due to more effective surface passivation by the CdS shell on the $Ge_{1-x}Sn_x$ cores, because Sn inclusion in the core without the shell did not result in a higher PL response (see above), whereas oxidation reduces luminescence. Considering the lattice parameters of the core and shell, doping the core with Sn leads to improved epitaxy (smaller lattice mismatch with the shell). This may produce improved crystal growth for core/shell nanocrystals with fewer defects within the crystals that can quench photoluminescence.

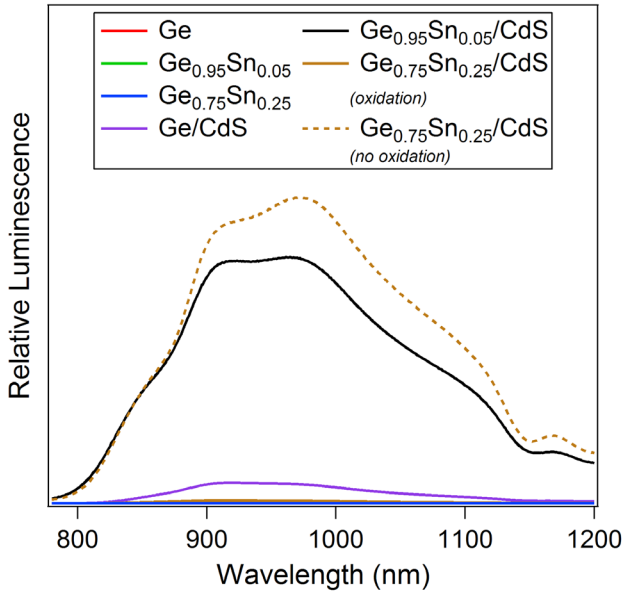

Figure 9. Relative near infrared photoluminescence (PL) spectra of the Ge and $Ge_{1-x}Sn_x$ cores and requisite core/shell nanocrystals. The intensity is normalized by the optical density at the excitation wavelength, λ_{exc} = 350 nm. The Ge, $Ge_{0.95}Sn_{0.05}$, $Ge_{0.75}Sn_{0.25}$, and oxidized $Ge_{0.75}Sn_{0.25}$/CdS samples overlap on this scale.

Excited-state lifetime measurements for the core/shell nanocrystals are shown in **Figure 10**. These measurements were performed on only the core/shell nanocrystals because the PL intensity of the core-only particles was too low to measure the lifetimes. The Ge/CdS nanocrystals yielded a lifetime of 4.1 µs, which is similar to the previous finding of Guo *et al.*[4] Upon incorporation of Sn in the Ge core, the PL lifetimes decreased to 2.8 and 1.0 µs for $Ge_{0.95}Sn_{0.05}$/CdS and $Ge_{0.75}Sn_{0.25}$/CdS, respectively. The observed decrease in PL lifetime along with higher steady state PL intensity in the core/shell nanocrystals could be indicative of a more direct band gap. However, there may be no correlation between the steady state PL intensity and the lifetimes of these materials. In order to correlate these two measurements, one would have to show the emitting states are the same for all types of nanocrystals; however, and unlike the case of coating cores of the exact same material but having different sizes, there is no reason to

assume this is the case for our series because they are based on chemically distinct cores (materials with different doping levels).

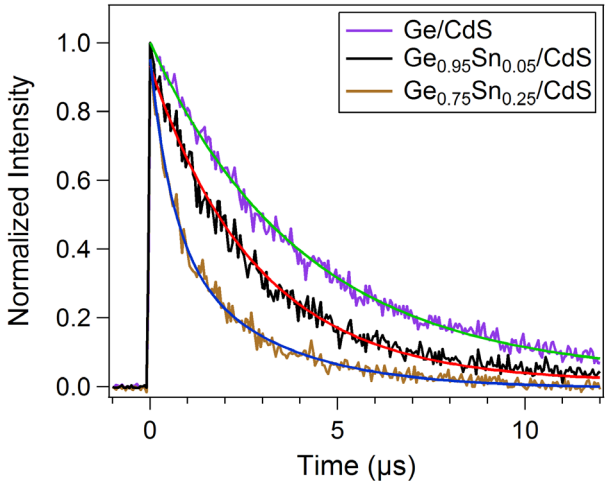

Figure 10. Time-resolved photoluminescence traces of Ge/CdS, $Ge_{0.95}Sn_{0.05}$/CdS, and $Ge_{0.75}Sn_{0.25}$/CdS core/shell nanocrystals. The decays of Ge/CdS and $Ge_{0.95}Sn_{0.05}$/CdS are single-exponential with lifetimes of 4.1 μs and 2.8 μs, respectively, while a double-exponential was used for $Ge_{0.75}Sn_{0.25}$/CdS, yielding an average lifetime of 1.0 μs.

Conclusion

$Ge_{1-x}Sn_x$ alloy nanocrystals and $Ge_{1-x}Sn_x$ core/shell nanocrystals were prepared *via* solution-based synthesis and characterized by XRD, TEM, Raman, optical, and X-ray photoelectron spectroscopy. Incorporation of Sn did not increase the PL intensity in the cores, but core/shell nanocrystals prepared using the Sn-doped cores and CdS shell show up to 15× enhanced PL when compared to Ge/CdS materials. This is explained by improved epitaxy between the lattice-expanded Sn-doped Ge cores and the structurally similar CdS shell, along with reduced surface oxidation. The combination of scalability and improved PL intensities make these $Ge_{1-x}Sn_x$ core/shell nanocrystals promising alternatives to other near infrared-active materials for use as functional materials in solar cells and LEDs. In addition, these nanocrystals

have potential as anode materials in advanced lithium ion batteries, and when combined with available biocompatibility steps (ligand exchange and surface-protection or encapsulation), as near-infrared luminescent markers in biological studies.

Supporting Information

TEM size distribution plots; Raman spectra of GeO_2 powder, Ge/CdS and $Ge_{1-x}Sn_x$/CdS core/shell nanocrystals; additional HAADF STEM images with registered EDX mapping for the $Ge_{0.75}Sn_{0.25}$/CdS nanocrystals; a table of Raman peak locations; XPS survey spectra; FTIR spectra of the nancrystals; and valence and conduction band offsets for Sn, Ge, and CdS. These materials are available free of charge via the internet at http://pubs.acs.org.

Acknowledgements

This research is supported by the U.S. Department of Energy, Office of Basic Energy Sciences, Division of Chemical Sciences, Geosciences, and Biosciences through the Ames Laboratory. Electron microscopy characterization was performed at Ames Laboratory's Sensitive Instrument Facility. Ames Laboratory is operated for the U.S. Department of Energy by Iowa State University under contract # DE-AC02-07CH11358. The authors thank Duane Johnson and Gordie Miller for comments. XPS work was performed at the Materials Analysis and Research Laboratory of the Iowa State University Office of Biotechnology. We thank Dapeng Jing for XPS measurements and discussions.

References

1. Vaughn, D. D., II; Schaak, R. E. Synthesis, Properties and Applications of Colloidal Germanium and Germanium-Based Nanomaterials. *Chem. Soc. Rev.* **2013**, *42*, 2861–2879.

2. Xu, C.; Gallagher, J.; Senaratne, C.; Menéndez, J.; Kouvetakis, J. Optical Properties of Ge-Rich $Ge_{1-x}Si_x$ Alloys: Compositional Dependence of the Lowest Direct and Indirect Gaps. *Phys. Rev. B* **2016**, *93*, 125206-1–125206-9.

3. Ruddy, D. A.; Johnson, J. C.; Smith, E. R.; Neale, N. R. Size and Bandgap Control in the Solution-Phase Synthesis of Near-Infrared-Emitting Germanium Nanocrystals. *ACS Nano* **2010**, *4*, 7459–7466.

4. Guo, Y.; Rowland, C. E.; Schaller, R. D.; Vela, J. Near-Infrared Photoluminescence Enhancement in Ge/CdS and Ge/ZnS Core/Shell Nanocrystals: Utilizing IV/II-VI Semiconductor Epitaxy. *ACS Nano* **2014**, *8*, 8334–8343.

5. Men, L.; White, M. A.; Andaraarachchi, H.; Rosales, B. A.; Vela, J. Synthetic Development of Low Dimensional Materials. *Chem. Mater.* **2017**, *29*, 168–175.

6. Esteves, R. J. A.; Ho, M. Q.; Arachchige, I. U. Nanocrystalline Group IV Alloy Semiconductors: Synthesis and Characterization of $Ge_{1-x}Sn_x$ Quantum Dots for Tunable Bandgaps. *Chem. Mater.* **2015**, *27*, 1559–1568.

7. Cheng, R.; Wang, W.; Gong, X.; Sun, L.; Guo, P.; Hu, H.; Shen, Z.; Han, G.; Yeo, Y.-C. Relaxed and Strained Patterned Germanium-Tin Structures: A Raman Scattering Study. *J. Solid State Sci.* **2013**, *2*, 138–145.

8. Gupta, S.; Magyari-Köpe, B.; Nishi, Y.; Saraswat, K. C. Achieving Direct Band Gap in Germanium through Integration of Sn Alloying and External Strain. *J. Appl. Phys.* **2013**, *113*, 073707-1–073707-7.

9. Lin, H.; Chen, R.; Huo, Y.; Kamins, T. I.; Harris, J. S. Raman Study of Strained $Ge_{1-x}Sn_x$ Alloys. *Appl. Phys. Lett.* **2011**, *98*, 261917-1–261917-3.

10. Gallagher, J.; Senaratne, C.; Kouvetakis, J.; Menendez, J. Compositional Dependence of the Bowing Parameter for the Direct and Indirect Band Gaps in $Ge_{1-y}Sn_y$ Alloys. *Appl. Phys. Lett.* **2014**, *105*, 142102-1–142102-5.

11. Senaratne, C. L.; Gallagher, J. D.; Xu, C.; Sims, P.; Menendez, J.; Kouvetakis, J. Doping of Direct Gap $Ge_{1-y}Sn_y$ Alloys to Attain Electroluminescence and Enhanced Photoluminescence. *ECS Trans.* **2015**, *69*, 157–164.

12. Stange, D.; Wirths, S.; Von Den Driesch, N.; Mussler, G.; Stoica, T.; Ikonic, Z.; Hartmann, J.; Mantl, S.; Grützmacher, D.; Buca, D. Optical Transitions in Direct-Bandgap $Ge_{1-x}Sn_x$ Alloys. *ACS Photonics* **2015**, *2*, 1539–1545.

13. Carolan, D.; Doyle, H. Efficient One-Pot Synthesis of Monodisperse Alkyl-Terminated Colloidal Germanium Nanocrystals. *J. Nanopart. Res.* **2014**, *16*, 2721-1–2721-8.

14. Carolan, D.; Doyle, H. Size Controlled Synthesis of Germanium Nanocrystals: Effect of Ge Precursor and Hydride Reducing Agent. *J. Nanomater.* **2015**, *16*, 156-1–156-9.

15. Chou, N. H.; Oyler, K. D.; Motl, N. E.; Schaak, R. E. Colloidal Synthesis of Germanium Nanocrystals Using Room-Temperature Benchtop Chemistry. *Chem. Mater.* **2009**, *21*, 4105–4107.

16. Codoluto, S. C.; Baumgardner, W. J.; Hanrath, T. Fundamental Aspects of Nucleation and Growth in the Solution-Phase Synthesis of Germanium Nanocrystals. *CrystEngComm* **2010**, *12*, 2903–2909.

17. Karatutlu, A.; Song, M.; Wheeler, A. P.; Ersoy, O.; Little, W. R.; Zhang, Y.; Puech, P.; Boi, F. S.; Luklinska, Z.; Sapelkin, A. V. Synthesis and Structure of Free-Standing Germanium Quantum Dots and Their Application in Live Cell Imaging. *RSC Adv.* **2015**, *5*, 20566–20573.

18. Lee, D. C.; Pietryga, J. M.; Robel, I.; Werder, D. J.; Schaller, R. D.; Klimov, V. I. Colloidal Synthesis of Infrared-Emitting Germanium Nanocrystals. *J. Am. Chem. Soc.* **2009**, *131*, 3436–3437.

19. Lu, X. M.; Korgel, B. A.; Johnston, K. P. High Yield of Germanium Nanocrystals Synthesized from Germanium Diiodide in Solution. *Chem. Mater.* **2005**, *17*, 6479–6485.

20. Zhang, Y.; Ersoy, O.; Karatutlu, A.; Little, W.; Sapelkin, A. Local Structure of Ge Quantum Dots Determined by Combined Numerical Analysis of EXAFS and XANES Data. *J. Synchrotron Radiat.* **2016**, *23*, 253–259.

21. Prabakar, S.; Shiohara, A.; Hanada, S.; Fujioka, K.; Yamamoto, K.; Tilley, R. D. Size Controlled Synthesis of Germanium Nanocrystals by Hydride Reducing Agents and Their Biological Applications. *Chem. Mater.* **2010**, *22*, 482–486.

22. Warner, J. H.; Tilley, R. D. Synthesis of Water-Soluble Photoluminescent Germanium Nanocrystals. *Nanotechnology* **2006**, *17*, 3745–3749.

23. Cosentino, S.; Torrisi, G.; Raciti, R.; Zimbone, M.; Crupi, I.; Mirabella, S.; Terrasi, A. Growth Kinetics of Colloidal Ge Nanocrystals for Light Harvesters. *RSC Adv.* **2016**, *6*, 38454–38462.

24. Ghosh, B.; Makoto, O.; Sakka, Y.; Shirahata, N. Reductant-Free Colloidal Synthesis of Near-IR Emitting Germanium Nanocrystals: Role of Primary Amine. *J. Nanosci. Nanotechnol.* **2014**, *14*, 2204–2210.

25. Shirahata, N. Solution-Processable White-Light-Emitting Germanium Nanocrystals. *J. Solid State Chem.* **2014**, *214*, 74–78.

26. Holmes, A. L.; Hutges, J.; Reckmann, A.; Muthuswamy, E.; Meerholz, K.; Kauzlarich, S. M. Probing Electronics as a Function of Size and Surface of Colloidal Germanium Nanocrystals. *J. Phys. Chem. C* **2015**, *119*, 5671–5678.

27. Muthuswamy, E.; Iskandar, A. S.; Amador, M. M.; Kauzlarich, S. M. Facile Synthesis of Germanium Nanoparticles with Size Control: Microwave versus Conventional Heating. *Chem. Mater.* **2013**, *25*, 1416–1422.

28. Muthuswamy, E.; Zhao, J.; Tabatabaei, K.; Amador, M. M.; Holmes, M. A.; Osterloh, F. E.; Kauzlarich, S. M. Thiol-Capped Germanium Nanocrystals: Preparation and Evidence for Quantum Size Effects. *Chem. Mater.* **2014**, *26*, 2138–2146.

29. Vaughn, D. D., II; Bondi, J. F.; Schaak, R. E. Colloidal Synthesis of Air-Stable Crystalline Germanium Nanoparticles with Tunable Sizes and Shapes. *Chem. Mater.* **2010**, *22*, 6103–6108.

30. Ruddy, D. A.; Erslev, P. T.; Habas, S. E.; Seabold, J. A.; Neale, N. R. Surface Chemistry Exchange of Alloyed Germanium Nanocrystals: A Pathway Toward Conductive Group IV Nanocrystal Films. *J. Phys. Chem. Lett.* **2013**, *4*, 416–421.

31. Armatas, G. S.; Kanatzidis, M. G. Mesoporous Compound Semiconductors from the Reaction of Metal Ions with Deltahedral $[Ge_9]^{4-}$ Clusters. *J. Am. Chem. Soc.* **2008**, *130*, 11430–11436.

32. Armatas, G. S.; Kanatzidis, M. G. High-Surface-Area Mesoporous Germanium from Oxidative Polymerization of the Deltahedral $[Ge_9]^{4-}$ Cluster: Electronic Structure Modulation with Donor and Acceptor Molecule. *Adv. Mater.* **2008**, *20*, 546–550.

33. Armatas, G. S.; Kanatzidis, M. G. Mesoporous Germanium-Rich Chalcogenido Frameworks with Highly Polarizable Surfaces and Relevance to Gas Separation. *Nat. Mater.* **2009**, *8*, 217–222.

34. Armatas, G. S.; Kanatzidis, M. G. Size Dependence in Hexagonal Mesoporous Germanium: Pore Wall Thickness versus Energy Gap and Photoluminescence. *Nano Lett.* **2010**, *10*, 3330–3336.

35. Bag, S.; Trikalitis, P. N.; Chupas, P. J.; Armatas, G. S.; Kanatzidis, M. G. Porous Semiconducting Gels and Aerogels from Chalcogenide Clusters. *Science* **2007**, *317*, 490–493.

36. Henderson, E. J.; Hessel, C. M.; Cavell, R. G.; Veinot, J. G. C. How Processing Atmosphere Influences the Evolution of GeO_2-Embedded Germanium Nanocrystals Obtained from the Thermolysis of Phenyl Trichlorogermane-Derived Polymers. *Chem. Mater.* **2010**, *22*, 2653–2661.

37. Hoffman, M.; Veinot, J. G. C. Understanding the Formation of Elemental Germanium by Thermolysis of Sol-Gel Derived Organogermanium Oxide Polymers. *Chem. Mater.* **2012**, *24*, 1283–1291.

38. Henderson, E. J.; Hessel, C. M.; Veinot, J. G. C. Synthesis and Photoluminescent Properties of Size-Controlled Germanium Nanocrystals from Phenyl Trichlorogermane-Derived Polymers. *J. Am. Chem. Soc.* **2008**, *130*, 3624–3632.

39. Henderson, E. J.; Seino, M.; Puzzo, D. P.; Ozin, G. A. Colloidally Stable Germanium Nanocrystals for Photonic Applications. *ACS Nano* **2010**, *4*, 7683–7691.

40. Henderson, E. J.; Veinot, J. G. C. Synthesis of Oxide Encapsulated and Freestanding Hydride Surface Terminated $Si_{1-x}Ge_x$ Nanocrystals. *Chem. Mater.* **2007**, *19*, 1886–1888.

41. Wu, J.; Sun, Y.; Zou, R.; Song, G.; Chen, Z.; Wang, C.; Hu, J. One-Step Aqueous Solution Synthesis of Ge Nanocrystals from GeO_2 Powders. *CrystEngComm* **2011**, *13*, 3674–3677.

42. Purkait, T. K.; Swarnakar, A. K.; De Los Reyes, G. B.; Hegmann, F. A.; Rivard, E.; Veinot, J. G. C. One-Pot Synthesis of Functionalized Germanium Nanocrystals from a Single Source Precursor. *Nanoscale* **2015**, *7*, 2241–2244.

43. Millo, O.; Balberg, I.; Azulay, D.; Purkait, T. K.; Swarnakar, A. K.; Rivard, E.; Veinot, J. G. C. Direct Evaluation of the Quantum Confinement Effect in Single Isolated Ge Nanocrystals. *J. Phys. Chem. Lett.* **2015**, *6*, 3396–3402.

44. Kim, C. H.; Im, H. S.; Cho, Y. J.; Jung, C. S.; Jang, D. M.; Myung, Y.; Kim, H. S.; Back, S. H.; Lim, Y. R.; Lee, C.-W.; Park, J. High-Yield Gas-Phase Laser Photolysis Synthesis of Germanium Nanocrystals for High-Performance Photodetectors and Lithium Ion Batteries. *J. Phys. Chem. C* **2012**, *116*, 26190–26196.

45. Kim, S.; Walker, B.; Park, S. Y.; Choi, H.; Ko, S.-J.; Jeong, J.; Yun, M. H.; Lee, J. C.; Kim, D. S.; Kim, J. Y. Size Tailoring of Aqueous Germanium Nanoparticle Dispersions. *Nanoscale* **2014**, *6*, 10156–10160.

46. Cho, Y. J.; Kim, C. H.; Im, H. S.; Myung, Y.; Kim, H. S.; Back, S. H.; Lim, Y. R.; Jung, C. S.; Jang, D. M.; Park, J. Germanium–Tin Alloy Nanocrystals for High-Performance Lithium Ion Batteries. *Phys. Chem. Chem. Phys.* **2013**, *15*, 11691–11695.

47. Shirahata, N.; Hirakawa, D.; Masuda, Y.; Sakka, Y. Size-Dependent Color Tuning of Efficiently Luminescent Germanium Nanoparticles. *Langmuir* **2013**, *29*, 7401–7410.

48. Nolan, B. M.; Chan, E. K.; Zhang, X.; Muthuswamy, E.; van Benthem, K.; Kauzlarich, S. M. Sacrificial Silver Nanoparticles: Reducing GeI_2 to Form Hollow Germanium Nanoparticles by Electroless Deposition. *ACS Nano* **2016**, *10*, 5391–5397.

49. Meng, A. C.; Fenrich, C. S.; Braun, M. R.; McVittie, J. P.; Marshall, A. F.; Harris, J. S.; McIntyre, P. C. Core/Shell Germanium/Germanium-Tin Nanowires Exhibiting Room Temperature Direct-and Indirect-Gap Photoluminescence. *Nano Lett.* **2016**, *16*, 7521–7529.

50. Biswas, S.; Doherty, J.; Saladukha, D.; Ramasse, Q.; Majumdar, D.; Upmanyu, M.; Singha, A.; Ochalski, T.; Morris, M. A.; Holmes, J. D. Non-Equilibrium Induction of Tin in Germanium: Towards Direct Bandgap $Ge_{1-x}Sn_x$ Nanowires. *Nat. Commun.* **2016**, *7*, 11405-1–11405-12.

51. Stoldt, C. R.; Haag, M. A.; Larsen, B. A. Preparation of Freestanding Germanium Nanocrystals by Ultrasonic Aerosol Pyrolysis. *Appl. Phys. Lett.* **2008**, *93*, 043125-1–043125-3.

52. Ma, X.; Wu, F.; Kauzlarich, S. M. Alkyl-Terminated Crystalline Ge Nanoparticles Prepared from NaGe: Synthesis, Functionalization and Optical Properties. *J. Solid State Chem.* **2008**, *181*, 1628–1633.

53. Wheeler, L. M.; Levij, L. M.; Kortshagen, U. R. Tunable Band Gap Emission and Surface Passivation of Germanium Nanocrystals Synthesized in the Gas Phase. *J. Phys. Chem. Lett.* **2013**, *4*, 3392–3396.

54. Gresback, R.; Holman, Z.; Kortshagen, U. Plasma Synthesis of Highly Monodisperse Ge Nanocrystals and Self-Assembly of Dense Nanocrystal Layers. *Mater. Res. Soc. Symp. Proc.* **2006**, *974*, 0974–CC05.

55. Gresback, R.; Holman, Z.; Kortshagen, U. Nonthermal Plasma Synthesis of Size-Controlled, Monodisperse, Freestanding Germanium Nanocrystals. *Appl. Phys. Lett.* **2007**, *91*, 093119-1–093119-3.

56. Wheeler, L. M.; Nichols, A. W.; Chernomordik, B. D.; Anderson, N. C.; Beard, M. C.; Neale, N. R. All-Inorganic Germanium Nanocrystal Films by Cationic Ligand Exchange. *Nano Lett.* **2016**, *16*, 1949–1954.

57 Warner, J. H. Solution-Phase Synthesis of Germanium Nanoclusters Using Sulfur. *Nanotechnology* **2006**, *19*, 5613–5619.

58. Zaitseva, N.; Dai, Z. R.; Grant, C. D.; Harper, J.; Saw, C. Germanium Nanocrystals Synthesized in High-Boiling-Point Organic Solvents. *Chem. Mater.* **2007**, *19*, 5174–5178.

59. Ramasamy, K.; Kotula, P. G.; Fidler, A. F.; Brumbach, M. T.; Pietryga, J. M.; Ivanov, S. A. Sn_xGe_{1-x} Alloy Nanocrystals: A First Step toward Solution-Processed Group IV Photovoltaics. *Chem. Mater.* **2015**, *27*, 4640–4649.

60. Barth, S.; Seifner, M. S.; Bernardi, J. Microwave-Assisted Solution–Liquid–Solid Growth of $Ge_{1-x}Sn_x$ Nanowires with High Tin Content. *Chem. Commun.* **2015**, *51*, 12282–12285.

61. Seifner, M. S.; Biegger, F.; Lugstein, A.; Bernardi, J.; Barth, S. Microwave-Assisted $Ge_{1-x}Sn_x$ Nanowire Synthesis: Precursor Species and Growth Regimes. *Chem. Mater.* **2015**, *27*, 6125–6130.

62. Tonkikh, A. A.; Zakharov, N. D.; Suvorova, A. A.; Eisenschmidt, C.; Schilling, J.; Werner, P. Cubic Phase Sn-Rich GeSn Nanocrystals in a Ge Matrix. *Cryst. Growth Des.* **2014**, *14*, 1617–1622.

63. Bodnarchuk, M. I.; Kravchyk, K. V.; Krumeich, F.; Wang, S.; Kovalenko, M. V. Colloidal Tin-Germanium Nanorods and Their Li-Ion Storage Properties. *ACS Nano* **2014**, *8*, 2360–2368.

64. D'Costa, V. R.; Cook, C. S.; Birdwell, A. G.; Littler, C. L.; Canonico, M.; Zollner, S.; Kouvetakis, J.; Menéndez, J. Optical Critical Points of Thin-Film $Ge_{1-y}Sn_y$ Alloys: A Comparative $Ge_{1-y}Sn_y/Ge_{1-x}Si_x$ Study. *Phys. Rev. B* **2006**, *73*, 125207-1–125207-16.

65. Li, S. F.; Bauer, M. R.; Menéndez, J.; Kouvetakis, J. Scaling Law for the Compositional Dependence of Raman Frequencies in SnGe and GeSi Alloys. *Appl. Phys. Lett.* **2004**, *84*, 867–869.

66. Dag, Ö.; Henderson, E. J.; Ozin, G. A. Synthesis of Nanoamorphous Germanium and Its Transformation to Nanocrystalline Germanium. *Small* **2012**, *8*, 921–929.

67. Robel, I.; Shabaev, A.; Lee, D. C.; Schaller, R. D.; Pietryga, J. M.; Crooker, S. A.; L. Efros, A.; Klimov, V. I. Temperature and Magnetic-Field Dependence of Radiative Decay in Colloidal Germanium Quantum Dots. *Nano Lett.* **2015**, *15*, 2685–2692.

68. Du, W.; Ghetmiri, S. A.; Conley, B. R.; Mosleh, A.; Nazzal, A.; Soref, R. A.; Sun, G.; Tolle, J.; Margetis, J.; Naseem, H. A. Competition of Optical Transitions between Direct and Indirect Bandgaps in $Ge_{1-x}Sn_x$. *Appl. Phys. Lett.* **2014**, *105*, 051104-1–051104-4.

69. Wirths, S.; Geiger, R.; Von Den Driesch, N.; Mussler, G.; Stoica, T.; Mantl, S.; Ikonic, Z.; Luysberg, M.; Chiussi, S.; Hartmann, J. Lasing in Direct-Bandgap GeSn Alloy Grown on Si. *Nat. photon.* **2015**, *9*, 88–92.

70. Esteves, R. J. A.; Hafiz, S.; Demchenko, D. O.; Özgür, Ü.; Arachchige, I. U. Ultra-Small $Ge_{1-x}Sn_x$ Quantum Dots with Visible Photoluminescence. *Chem. Commun.* **2016**, *52*, 11665–11668.

71. Hafiz, S. A.; Esteves, R. J. A.; Demchenko, D. O.; Arachchige, I. U.; Özgür, U. M. Energy Gap Tuning and Carrier Dynamics in Colloidal $Ge_{1-x}Sn_x$ Quantum Dots. *J. Phys. Chem. Lett.* **2016**, *7*, 3295–3301.

72. Pezzoli, F.; Giorgioni, A.; Patchett, D.; Myronov, M. Temperature-Dependent Photoluminescence Characteristics of GeSn Epitaxial Layers. *ACS Photonics* **2016**, *3*, 2004–2009.

73. Chen, Y.; Vela, J.; Htoon, H.; Casson, J. L.; Werder, D. J.; Bussian, D. A.; Klimov, V. I.; Hollingsworth, J. A. "Giant" Multishell CdSe Nanocrystal Quantum Dots With Suppressed Blinking. *J. Am. Chem. Soc.* **2008**, *130*, 5026–5027.

74. Tan, R.; Yuan, Y.; Nagaoka, Y.; Eggert, D.; Wang, X.; Thota, S.; Guo, P.; Yang, H.; Zhao, J.; Chen, O. Monodisperse Hexagonal Pyramidal and Bipyramidal Wurtzite CdSe-CdS Core–Shell Nanocrystals. *Chem. Mater.* **2017**, *29*, 4097–4108.

75. Sainz, M.; Pérez-Rontomé, C.; Ramos, J.; Mulet, J. M.; James, E. K.; Bhattacharjee, U.; Petrich, J. W.; Becana, M. Plant Hemoglobins May Be Maintained in Functional Form by Reduced Flavins in the Nuclei, and Confer Differential Tolerance to Nitro-Oxidative Stress. *Plant J.* **2013**, *76*, 875–887.

76. Olesinski, R. W.; Abbaschian, G. J. The Ge–Sn (Germanium–Tin) System. *Bull. Alloy Phase Diagrams* **1984**, *5*, 265–271.

77. Rojas-Lopez, M.; Navarro-Contreras, H.; Desjardins, P.; Gurdal, O.; Taylor, N.; Carlsson, J.; Greene, J. Raman Scattering from Fully Strained $Ge_{1-x}Sn_x$ ($x <= 0.22$) Alloys Grown on Ge (001) 2x1 by Low-Temperature Molecular Beam Epitaxy. *J. Appl. Phys.* **1998**, *84*, 2219–2223.

78. Su, S.; Wang, W.; Cheng, B.; Hu, W.; Zhang, G.; Xue, C.; Zuo, Y.; Wang, Q. The Contributions of Composition and Strain to the Phonon Shift in Alloys. *Solid State Commun.* **2011**, *151*, 647–650.

79. Gupta, R.; Xiong, Q.; Mahan, G. D.; Eklund, P. C. Surface Optical Phonons in Gallium Phosphide Nanowires. *Nano Lett.* **2003**, *3*, 1745–1750.

80. Tschirner, N.; Lange, H.; Schliwa, A.; Biermann, A.; Thomsen, C.; Lambert, K.; Gomes, R.; Hens, Z. Interfacial Alloying in CdSe/CdS Heteronanocrystals: A Raman Spectroscopy Analysis. *Chem. Mater.* **2012**, *24*, 311–318.

81. Lange, H.; Artemyev, M.; Woggon, U.; Thomsen, C. Geometry Dependence of the Phonon Modes in CdSe Nanorods. *Nanotechnology* **2009**, *20*, 045705-1–045705-5.

82. Micoulaut, M.; Cormier, L.; Henderson, G. The Structure of Amorphous, Crystalline and Liquid GeO_2. *J. Phys.: Condens. Matter* **2006**, *18*, R753–R784.

83. Li, J. J.; Wang, Y. A.; Guo, W.; Keay, J. C.; Mishima, T. D.; Johnson, M. B.; Peng, X. Large-Scale Synthesis of Nearly Monodisperse CdSe/CdS Core/Shell Nanocrystals Using Air-Stable Reagents via Successive Ion Layer Adsorption and Reaction. *J. Am. Chem. Soc.* **2003**, *125*, 12567–12575.

84. Lopez, F. J.; Givan, U.; Connell, J. G.; Lauhon, L. J. Silicon Nanowire Polytypes: Identification by Raman Spectroscopy, Generation Mechanism, and Misfit Strain in Homostructures. *ACS Nano* **2011**, *5*, 8958–8966.

85. Mélinon, P.; Masenelli, B.; Tournus, F.; Perez, A. Playing With Carbon and Silicon at the Nanoscale. *Nat. Mater.* **2007**, *6*, 479–490.

86. Segarra, C.; Rajadell, F.; Climente, J. I.; Planelles, J. Influence of Polytypism on the Electronic Structure of CdSe/CdS and CdSe/CdSe Core/Shell Nanocrystals. *J. Phys. Chem. C* **2017**, *121*, 6386–6392.

87. Bertoni, G.; Grillo, V.; Brescia, R.; Ke, X.; Bals, S.; Catellani, A.; Li, H.; Manna, L. Direct Determination of Polarity, Faceting, and Core Location in Colloidal Core/Shell Wurtzite Semiconductor Nanocrystals. *ACS Nano* **2012**, *6*, 6453–6461.

88. McBride, J.; Treadway, J.; Feldman, L. C.; Pennycook, S. J.; Rosenthal, S. J. Structural Basis for Near Unity Quantum Yield Core/Shell Nanostructures. *Nano Lett.* **2006**, *6*, 1496–1501.

89. Rosenthal, S. J.; McBride, J.; Pennycook, S. J.; Feldman, L. C. Synthesis, Surface Studies, Composition and Structural Characterization of CdSe, Core/Shell and Biologically Active Nanocrystals. *Surf. Sci. Rep.* **2007**, *62*, 111–157.

90. Guo, Y.; Marchuk, K.; Sampat, S.; Abraham, R.; Fang, N.; Malko, A. V.; Vela, J. Unique Challenges Accompany Thick-Shell CdSe/nCdS (n>10) Nanocrystal Synthesis. *J. Phys. Chem. C* **2012**, *116*, 2791–2800.
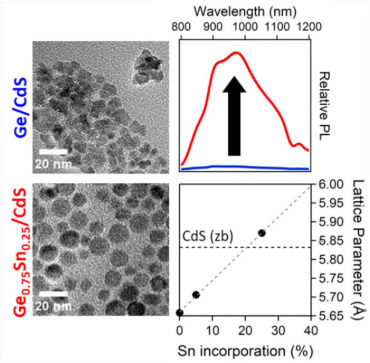
TOC Figure